Cooperation between intrinsically disordered and ordered regions of Spt6 regulates nucleosome and Pol II CTD binding, and nucleosome assembly

Aiste Kasiliauskaite [ID][1,2], Karel Kubicek[1,3], Tomas Klumpler[1], Martina Zanova[1,3], David Zapletal[1,2], Eliska Koutna[4,5], Jiri Novacek[1] and Richard Stefl [ID][1,2,*]

[1]CEITEC–Central European Institute of Technology, Masaryk University, Brno CZ-62500, Czech Republic, [2]National Centre for Biomolecular Research, Faculty of Science, Masaryk University, Brno CZ-62500, Czech Republic, [3]Department of Condensed Matter Physics, Faculty of Science, Masaryk University, Brno CZ-61137, Czech Republic, [4]Institute of Organic Chemistry and Biochemistry of the Czech Academy of Sciences, Prague, Czech Republic and [5]Department of Cell Biology, Faculty of Science, Charles University, Prague, Czech Republic

ABSTRACT

Transcription elongation factor Spt6 associates with RNA polymerase II (Pol II) and acts as a histone chaperone, which promotes the reassembly of nucleosomes following the passage of Pol II. The precise mechanism of nucleosome reassembly mediated by Spt6 remains unclear. In this study, we used a hybrid approach combining cryo-electron microscopy and small-angle X-ray scattering to visualize the architecture of Spt6 from *Saccharomyces cerevisiae*. The reconstructed overall architecture of Spt6 reveals not only the core of Spt6, but also its flexible N- and C-termini, which are critical for Spt6's function. We found that the acidic N-terminal region of Spt6 prevents the binding of Spt6 not only to the Pol II CTD and Pol II CTD-linker, but also to pre-formed intact nucleosomes and nucleosomal DNA. The N-terminal region of Spt6 self-associates with the tSH2 domain and the core of Spt6 and thus controls binding to Pol II and nucleosomes. Furthermore, we found that Spt6 promotes the assembly of nucleosomes *in vitro*. These data indicate that the cooperation between the intrinsically disordered and structured regions of Spt6 regulates nucleosome and Pol II CTD binding, and also nucleosome assembly.

GRAPHICAL ABSTRACT
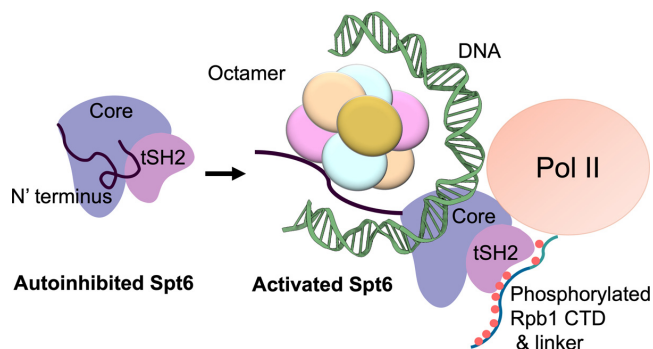
INTRODUCTION

Spt6 is a highly-conserved protein that is known to be a transcription elongation factor and histone chaperone, as well as mRNA processing and DNA repair factor (1–9). Mutations in *Saccharomyces cerevisiae* SPT6 cause genome-wide changes in histone occupancy and impair several histone modifications (10–14). In the absence of functional Spt6, transcription generates nucleosome loss and nucleosome misplacing, and it can be partially compensated by the elevated activity of non-transcription-coupled histone chaperones (6,12,15,16). Interestingly, deletion of the RNA polymerase II (Pol II) binding domain in yeast Spt6 leads to reduced occupancy of Spt6 throughout transcribed genes (17). Spt6 plays several mechanistically distinct roles during transcription and chromatin remodelling events. Current models suggest that Spt6 accomplishes this by binding to RNA polymerase II during transcription and then uses its multiple functional domains to coordinate the activities of transcription elongation and mRNA processing ma-

chinery with the reassembly of chromatin after the passage of Pol II ([18]). Spt6 is a 1451 amino acid residue, 168 kDa protein (Figure [1]) composed of a structured protein core (residues 336–1219) with an acidic N-terminal region that has sequence features of intrinsically disordered proteins, and a C-terminal tSH2 domain bridged by a 28-residue linker. Five domains of the core of Spt6 carry scaffold and specific functions, including DNA binding ([19,20]), tSH2 is implicated in the recognition of phosphorylated Pol II CTD and its linker ([20–23]), which could be important for the recruitment and/or retention of Spt6 on genes, and a disordered N-terminal region. Spt6 has been shown to assemble nucleosomes and bind histones ([24–26]).

To advance the mechanistic understanding of Spt6's function, we have determined the structural basis for cooperation between the intrinsically disordered and structured regions of Spt6, which both contribute to the regulation of binding to Pol II CTD and nucleosomes. We also demonstrate that not only the histone chaperoning activity of the acidic N-terminal region, but also the DNA-binding properties of the Spt6 core, are important to stimulate nucleosome assembly.

MATERIALS AND METHODS

Plasmids

pET151-D/Topo vectors containing *S. cerevisiae* Spt6, Spt6-ΔC, or tSH2 were kindly provided by the C.P. Hill laboratory (University of Utah School of Medicine, Salt Lake City, United States; [19]). Spt6 (lacks 238 amino-terminal residues; 239–1451; Figure [1]), ΔN-Spt6 (298–1451), ΔN-Spt6-ΔC (298–1259), and mutated versions of tSH2 (1247–1451) were generated using the polymerase incomplete primer extension (PIPE) method ([27]). Plasmids bearing the *Xenopus laevis* H2A–H2B and H3–H4 genes were kindly provided by S. Bilokapic and M. Halic (St. Jude Children's Research Hospital, Memphis, United States; [28]). Plasmid pQTEV-ASF1A was kindly provided by K. Buessow (Addgene plasmid #31591; http://n2t.net/addgene:31591;RRID:Addgene 31591).

Protein expression and purification

The dimer of H2A–H2B and tetramer of H3–H4 were expressed and purified as previously described ([29]). The histone octamer was formed by mixing the dimer and tetramer in a 3:1 molar ratio in 25 mM HEPES/NaOH, pH 7.5, 2M NaCl, 2 mM DTT buffer. After overnight incubation in a cold room (4°C), the histone octamer was purified from the unincorporated components in a size-exclusion Superdex 200 Increase 10/300 GL column (GE Healthcare).

All the Spt6 protein variants were expressed in BL21 codon plus (RIL) *E. coli* cells (Stratagene). Bacterial cultures were grown in an autoinduction medium containing the appropriate antibiotics. When the OD_{600} reached ∼0.4, the culture was shifted to 18°C. After overnight expression, cells were harvested by centrifugation at 7878 × *g* and resuspended in lysis buffer (50 mM sodium-phosphate, pH 8.0, 500 mM NaCl, 20 mM imidazole, 5% (v/v) glycerol, 2 mM β- mercaptoethanol, benzonase, and protease inhibitors). Cell pellets were lysed by sonication using a

Vibra-Cell ultrasonic homogenizer (Sonics). The lysate was cleared by centrifugation at 21 036 × *g*. The cleared supernatants were applied to nickel agarose resin and eluted in elution buffer (50 mM sodium-phosphate, pH 8.0, 100 mM NaCl, 300 mM imidazole, 5% (v/v) glycerol, 2 mM β-mercaptoethanol), immediately followed by purification in a heparin column (5 ml HiTrap Heparin; GE Healthcare). Fractions containing Spt6 were pooled and mixed with TEV protease. The mixtures were dialysed overnight against cleavage buffer (50 mM sodium-phosphate, pH 8.0, 100 mM NaCl, 5% (v/v) glycerol, 2 mM β-mercaptoethanol). The proteins were then applied to a 5 ml HisTrap column (GE Healthcare) equilibrated with the cleavage buffer to remove uncleaved proteins, the cleaved His tag and TEV protease. The flow-through was collected, concentrated, and further purified in a size-exclusion Superdex 200 Increase 10/300 (GE Healthcare) column equilibrated with 25 mM sodium-phosphate, pH 7.5, 300 mM NaCl, 0.5 mM EDTA, 1 mM DTT. Pure peak fractions containing Spt6 were pooled, concentrated, aliquoted, flash frozen and stored at − 80°C until use. All purification steps were performed at 4°C. The protein samples were analysed by 18% SDS-PAGE after each purification step.

Histone chaperone Asf1 was expressed in BL21 Rosetta (DE3) competent cells (Novagen). Bacterial cultures were grown in LB medium containing the appropriate antibiotics. When the OD_{600} reached ∼0.6, the culture was shifted to 20°C. After overnight expression, cells were harvested by centrifugation at 7878 × *g* then resuspended in lysis buffer (20 mM TRIS-HCl, pH 8.0, 500 mM NaCl, 10 mM imidazole, 0.01% (v/v) NP-40). Cell pellets were lysed by sonication using a Vibra-Cell ultrasonic homogenizer (Sonics). The lysate was cleared by centrifugation at 21036 × *g*. The cleared supernatants were applied to nickel agarose resin and eluted in elution buffer (20 mM Tris–HCl, pH 8.0, 100 mM NaCl, 300 mM imidazole), immediately followed by application to a 1 ml HiTrap Q HP column (GE Healthcare) and elution over an NaCl gradient. Fractions containing Asf1 were pooled, concentrated and further purified in a size-exclusion Superdex 200 Increase 10/300 (GE Healthcare) column equilibrated with 25 mM HEPES/NaOH pH 7.5, 2 M NaCl, 1 mM DTT. Peak fractions containing Asf1 were pooled, concentrated and used for the nucleosome assembly assay. SDS page analyses of all purified proteins is shown in Supplementary Figure S1. Protein concentrations were determined by ultraviolet absorption.

DNA preparation

DNA of 149 bp for nucleosome reconstitution was PCR amplified from a plasmid containing the Widom 601 DNA sequence. Large-scale (10 ml) PCR reactions were performed with the PCR primers listed in Supplementary Table S1. The reaction was distributed into PCR tubes (100 µl per tube) and PCR was conducted with the following steps: 1. 95°C for 1 min, 2. 95°C for 30 s, 3. 55°C for 30 s, 4. 72°C for 40 s, cycle between steps 2 and 4, 30 times, 5. 72°C for 5 min, 6. pause at 4°C. PCR products were pooled, ethanol precipitated, and resuspended in 1 ml of 15 mM Tris pH 7.5, 500 mM NaCl, 1 mM DTT. DNA was further purified with a MonoQ 1ml column (GE Healthcare).
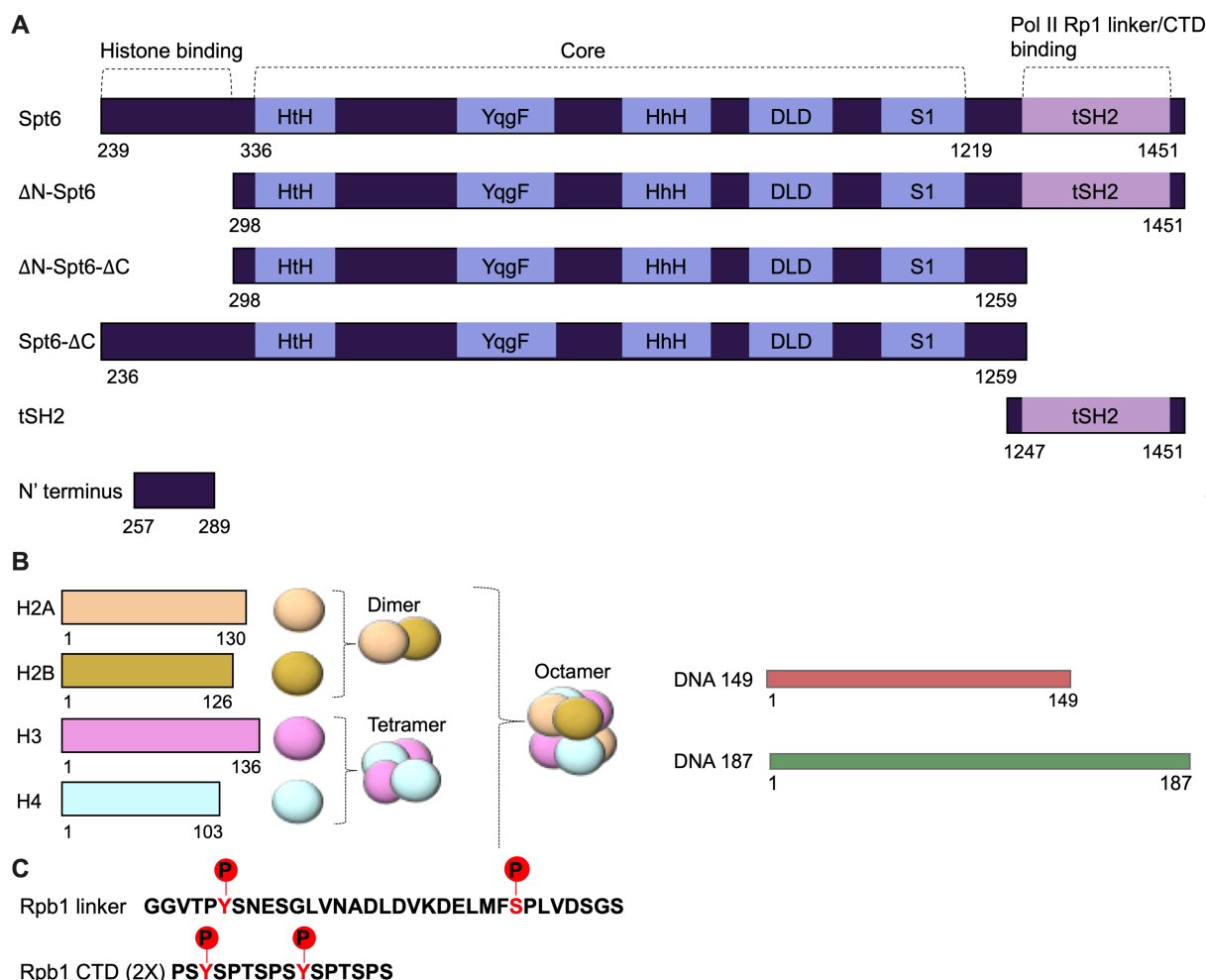
Figure 1. Schematic representation. (**A**) Domain organization of Spt6 and its variants used in this study. Residues for the N' terminus, core, tSH2 domain and different constructs of Spt6 are indicated. The core consists of five domains: HtH, helix-turn-helix domain; YqgF, looks similar to the RuvC catalytical domain; HhH, helix-hairpin-helix domain; DLD, death-like domain; S1 domain. Pictograms correspond to the flexible N' terminus, core, and tSH2 domain. (**B**) Cartoon representation of histones and DNA used for nucleosome reconstitution, binding and assembly assay. (**C**) Peptide sequences of Pol II Rpb1 linker and CTD used in binding studies. The residues of the peptides in red indicate phosphorylations

Peak fractions were pooled and concentrated by ethanol precipitation. DNA was resuspended in 15 mM HEPES-NaOH, pH 7.5, 2 M NaCl, 1 mM DTT. DNA of 187 bp for the nucleosome assembly assay was purchased from Active Motif.

Nucleosome reconstitution

Nucleosomes were reconstituted using the purified octamers and a 149 bp DNA fragment harboring the 601-nucleosome strong positioning sequence. Histone octamer and DNA were mixed in a 1:1.1 molar ratio and were reconstituted using a salt gradient and double dialysis bag as previously described (30). All nucleosome reconstitution steps were performed at 4°C. The reconstitution results were analysed in a 6% native PAGE run in 0.5× TBE buffer at 120 V in the cold room. The gels were stained with SYBR gold (Thermo Fisher Scientific). Freshly reconstituted nucleosomes were concentrated with Amicon Ultra-0.5 centrifugal filters MWCO 10 000 (Sigma Aldrich).

Fluorescence anisotropy binding assays

5,6-FAM-labelled peptides corresponding to the N-terminal region of Spt6 (*S.c.* Spt6 residues 257–289), phosphorylated Pol II Rpb1 linker (GGVTPpYSNESG LVNADLDVKDELMFpSPLVDSGS), and tyrosine-phosphorylated Pol II CTD (PSpYSPTSPSpYSPTSPS) were purchased from Caslo ApS. Samples of all the studied Spt6 variants were transferred to the binding buffer (15 mM Tris/Cl pH 7.5, 100 mM NaCl, pH 7.5, 1 mM DTT) by size-exclusion chromatography, and titrated against a constant concentration (0.3 nM) of fluorescently labeled peptides at 25°C, as described previously (31). The measurements were conducted in a FluoroLog-3 spectrofluorometer (Horiba Jobin- Yvon Edison). The instrument was equipped with a thermostatic cell holder with a Neslab RTE7 water bath (Thermo Scientific). Samples were excited with vertically polarized light at 467 nm, and both vertical and horizontal emissions were recorded at 516 nm. The experiments were performed in technical triplicates. Anisotropy data were plotted as a function of protein concentration and fitted

to a single-site saturation with non-specific binding model using GraphPad Prism Version 9.

DNA/nucleosome binding experiments

DNA or nucleosome and different variants of Spt6 were incubated in an EMSA buffer (25 mM HEPES/NaOH pH 7.5, 100 mM NaCl, 1 mM DTT) for 1h on ice. Each reaction contained 0.5 pmol DNA or nucleosome and increasing amounts of Spt6 (0, 0.5, 1, 2, 4, 8, 16, 32 pmol). Reactions were analyzed by native 6% 0.5× Tris–borate–EDTA (TBE) PAGE, the final amount of DNA or nucleosome added to the gel was 1 pmol. Gels were run at 120 V for 2h at 4°C and stained with SYBR Gold (Invitrogen). Identification of proteins from gel bands was done using liquid chromatography with tandem mass spectrometry (LC–MS/MS).

Nucleosome assembly experiments

Histones were mixed with increasing amounts of different variants of Spt6 (molar ratio 1:1, 1:2, 1:4) in octamer buffer (15 mM HEPES/NaOH pH 7.5, 2 M NaCl, 1 mM DTT), and incubated for 30 min on ice. The mixtures were added to 187 bp DNA in a low-salt buffer (20 mM HEPES/NaOH pH 7.5, 100 mM NaCl, 1 mM DTT), and incubated for 10 min at 37°C. The final molar ratio between the histones octamer and DNA was 0.4:1. Reactions were analyzed by native 6% 0.5× TBE PAGE, the final amount of DNA added to the gel was 1 pmol. Gels were run at 120 V for 2 h at 4°C and stained with SYBR Gold (Invitrogen). Negative controls of nucleosome assembly assay were performed in the same manner. The amounts and concentrations of all components were kept the same. The concentrations of Asf1 corresponded to the concentrations of Spt6.

Microscale thermophoresis

Microscale Thermophoresis was performed in a NanoTemper Monolith NT.115 apparatus (NanoTemper Technologies). Histones (dimer H2A–H2B and tetramer H3–H4 protein) were labelled with the Monolith NT Protein labelling kit RED-tris-NTA 2nd generation kit (NanoTemper Technologies) according to the manufacturer's protocol. Either 10 μl of 10 nM labelled H2A–H2B or 10 nM labelled H3–H4 were incubated with 10 μl of increasing concentrations of Spt6 in 20 mM HEPES, pH 7.5. Samples were then loaded into standard glass capillaries (Monolith NT Capillaries, NanoTemper Technologies) and the MST analysis was performed (the settings for the light-emitting diode and infrared laser were 80%). The data were analyzed using the software MO.Affinity Analysis (NanoTemper Technologies).

Protein identification from 1D gel bands by LC–MS/MS

After destaining and washing procedures, the proteins in the excised bands were subjected to reduction with dithiothreitol, alkylation with iodoacetamide, and then incubated with trypsin (sequencing grade; Promega) for 1 h at 40°C. Tryptic peptides were extracted from the gels and analyzed by LC–MS/MS using RSLCnano system connected to Orbitrap Exploris (Thermo Fisher Scientific). MS/MS data were searched against a custom database of relevant protein sequences in combination with cRAP contaminant database using an in-house Mascot search engine (Matrixscience; version 2.6). Carbamidomethylation (C), deamidation (N,Q) and oxidation (M) were set as variable modifications in all searches.

Single-particle Cryo-EM sample vitrification

The 3.5 μl of 0.15 mg/ml of Spt6 was applied to freshly glow-discharged TEM grids (Quantifoil, Cu, 300 mesh, R2/1) and vitrified in liquid ethane using a ThermoFisher Scientific Vitrobot Mark IV (4°C, 100% rel. humidity, 30 s waiting time, 3 s blotting time). The grids were subsequently mounted into Autogrid cartridges and loaded into a Titan Krios (ThermoFisher Scientific) transmission electron microscope for data acquisition.

Cryo-EM data acquisition

The Spt6 data were collected using a Titan Krios (ThermoFirsher Scientific) transmission electron microscope operated at 300 kV using SerialEM software (32). The data was acquired at the K2 (Gatan) direct electron detector operating in electron counting mode and positioned behind the Gatan Imaging Filter (GIF). The energy-selecting slit was set to 10 eV. The data from 5 s exposure were saved as a set of 40 frames comprising the overall dose of 55 e/Å^2. Micrographs were collected at the calibrated pixel size of 0.828 Å/px and the dataset consisted of 13 807 movies.

Cryo-EM data processing

The movies were first corrected for the drift during data acquisition using the program MotionCor2 (33), and the CTF parameters were estimated using GCTF (34). The images with astigmatism larger than 2500 Å and estimated resolution worse than 4.5 Å (based on the CTF fit analysis) were excluded. A set of 100 micrographs was randomly selected from the dataset for manual particle picking using the program e2boxer.py (35). The manually picked particles were used for generating the model for automated particle picking using the program Cryolo (36). The overall number of 160 769 particles were automatically selected and reference-free 2D classification was used to remove most of the false-positive picks and damaged particles using the program Relion3.1 (37). From the 2D classification, 17 741 particles were provided as input for cryoSPARC's Template Picker tool, and the whole dataset was further processed using the cryoSPARC platform (38). In total 2 995 892 particles were extracted from the full dataset and subsequent 2D classification provided 718 639 particles that were used for initial model determination and 3D refinement of the Spt6 electron map.

Cryo-EM model building and refinement

Initial PDB coordinates of the Spt6 structure comprising residues 298–1248 were produced from PDBs of a crystal
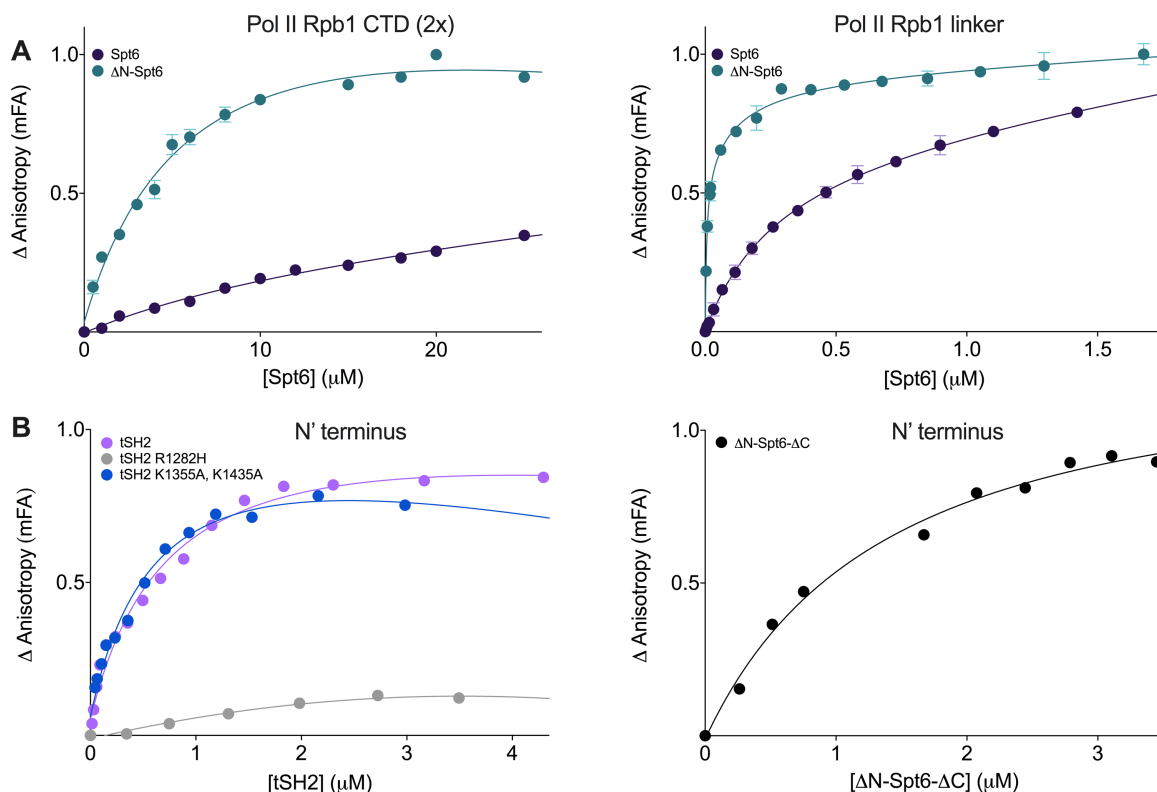
Figure 2. N-terminal region of Spt6 disrupts binding with Pol II and interacts with tSH2 domain and Spt6 core when added in trans. (**A**) Fluorescence anisotropy titration of phosphorylated Rpb1 CTD and Rpb1 linker peptides with Spt6 and ΔN-Spt6. Left panel – Rpb1 CTD binding with Spt6 lacking the flexible N-terminal region (cyan) $K_D \sim 6.7 \pm 1.56$ μM; Spt6 (violet) $K_D \sim$ n.d., not detected. Right panel – Rpb1 linker binding with Spt6 lacking the flexible N-terminal region (cyan) $K_D \sim 11 \pm 2.2$ nM, Spt6 (violet) $K_D \sim 290 \pm 70$ nM. Data represent means ± SD of technical triplicates. Normalized fluorescence anisotropy is plotted as a function of protein concentration. The data were normalized for visualization purposes and the experimental isotherms were fitted to a single-site saturation with non-specific binding model. (**B**) Fluorescence anisotropy titration shows that (left panel) N' terminus binds to wild-type tSH2 (purple) $K_D \sim 0.79 \pm 0.20$ μM, tSH2 variant with K1355A, K1435A double amino-acid substitutions (blue) $K_D \sim 0.67 \pm 0.39$ μM, tSH2 variant with R1282H substitution (grey) $K_D \sim$ n.d., not detected. ΔN-Spt6-ΔC associates with its N' terminus (added in trans) with a $K_D \sim$ 1.5 ± 0.7 μM (black, right panel). Points represent the mean ± SD of technical triplicates. The data were normalized for visualization purposes and the experimental isotherms were fitted to a single-site saturation with non-specific binding model

structure of Spt6, namely 3PSI and 3PSF. The PDB and the sharpened cryo-EM density map were imported into the program Coot (39) and the tool 'Real Space Refine Zone' was used to achieve optimal fit of the PDB coordinates within the map. Low-resolution regions of the map (regions corresponding to residues 1226–1243 and the S1 domain) were also excluded from the PDB and were docked with a rigid body approach using Phenix (40) once the fit of the well-resolved regions exhibited no clashes and deviations as identified by Coot and other validation tools (*vide infra*). The conformation of the PDB coordinates was validated using the tools 'Ramachandran Plot', 'Rotamer Analysis' and 'Density Analysis'. The structure obtained with Coot optimization was subjected to further structure refinement with Phenix software (40) and Isolde (41). MolProbity (42) was used to provide the overall refinement and structural statistics.

Small angle X-ray scattering measurements (SAXS)

The SAXS data were collected at the EMBL P12 beamline of the storage ring PETRA III (DESY, Hamburg, Germany) using a robotic sample changer at $\lambda = 0.124$ nm.

The scattering from Spt6 solutions and respective solvents was recorded at the Pilatus 2M pixel detector, radially averaged and processed using standard procedures. Twenty independent frames of a 50 ms exposure were collected for each sample and automatically radially averaged and solvent subtracted as implemented at beamline P12. Three solute concentrations were measured at 15°C or 20°C. Datapoints with $q < 0.008$ and $q > 3$ Å^{-1} (where $q = 4\pi\sin(\theta)/\lambda$) were truncated. The 5 mg/ml dataset was selected for further analysis as the curve with less noise for Spt6 and Spt6-ΔC. The 0.8 mg/ml dataset was selected for further analysis for the ΔN-Spt6 construct, because the curve was less affected by aggregation. Integral structural parameters were determined using PRIMUS/qt ATSAS v.2.8.4 (43). The *ab initio* modelling for superimposition with the atomic model was performed with DAMMIN ATSAS v.2.8.4, where the computation mode was set to 'slow', and all other parameters were kept at their default. Rigid body modeling was performed with *CORAL* ATSAS 2.8.4 (44) using the crystal structure of the Spt6 substructures (PDB ID: 3PSK, 3PSI, 3PSJ) as rigid bodies and amending them with chains of dummy residues to represent the fragments not present in the crystal. Protein flexibility was evaluated using EOM 2.0
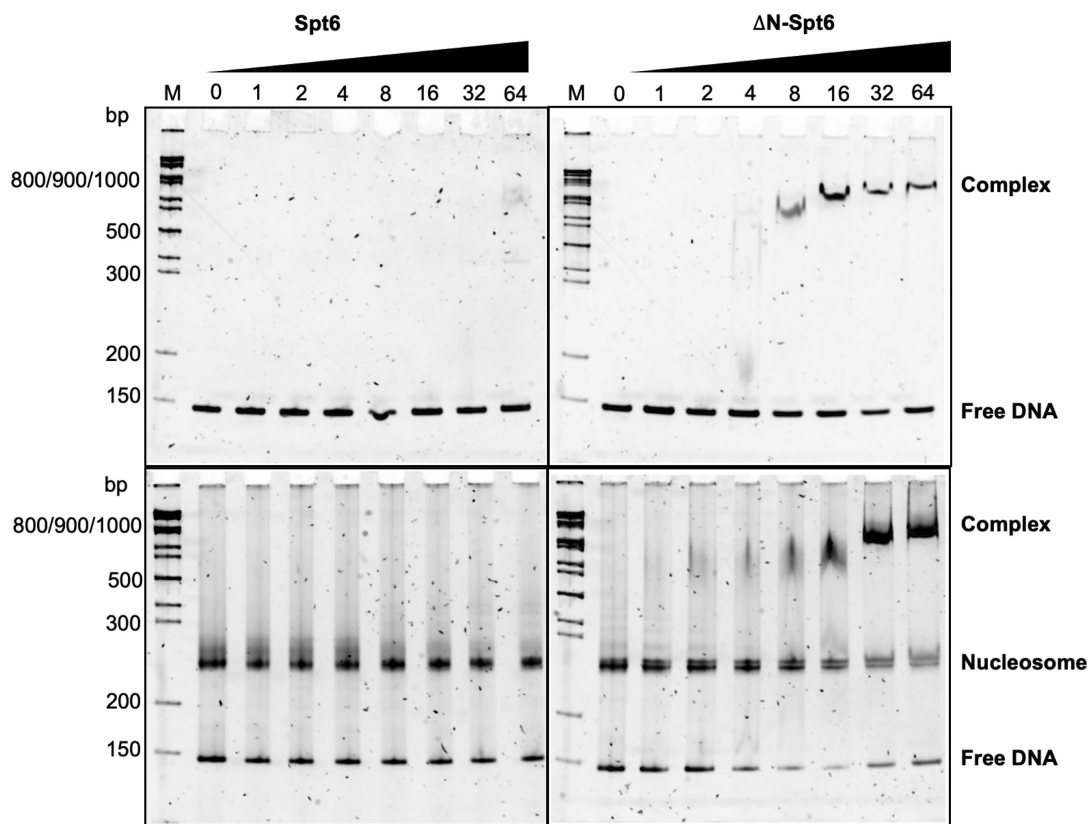
Figure 3. N-terminal part of Spt6 disrupts binding with DNA and nucleosome. EMSAs reveal the formation of ΔN-Spt6 complexes with DNA (top panel) or the nucleosome (bottom panel). A constant amount of 1 pmol of DNA and nucleosome was used with increasing molar ratio of different Spt6 variants. All experiments were repeated at least twice with similar results

(45). UCSF ChimeraX was used for graphical representation (46).

RESULTS

The N-terminal region of Spt6 autoregulates binding to Pol II Rpb1 CTD and Rpb1 linker

The tSH2 of Spt6 has been shown to interact with the Pol II Rpb1 linker (22) and with the Pol II Rpb1 CTD that bears different phospho-patterns (23), which could be important for the recruitment and/or retention of Spt6 on genes (17,47). Here, we probed Spt6 and Spt6 lacking the N-terminal region (ΔN-Spt6; Figure 1) for Rpb1 CTD and Rpb1 linker binding activity in a quantitative fluorescence anisotropy binding assay (Figure 2; Supplementary Figure S2). Spt6 has an acidic intrinsically disordered region (IDR) at the N-terminal region that is needed for gel shift of nucleosomes by Spt6 (26) and has often been removed in the previous functional and structural studies. Here, we wondered whether the N-terminal region has a role in Pol II Rpb1 CTD binding. We found that ΔN-Spt6 binds Rpb1 CTD with a K_D of 6.7 ± 1.56 μM and Rpb1 linker with a K_D of 11 ± 2.2 nM. The binding affinities of ΔN-Spt6 (containing the Spt6 core and tSH2) were similar to the binding affinities of isolated tSH2 domain (22,23,48). Surprisingly, we also found that Spt6 exhibited an undetectable and significantly weaker binding to the Rpb1 CTD and Rpb1 linker, respectively, when compared to ΔN-Spt6 (Figure 2).

This suggests that the N-terminal region of Spt6 may contain sequences that cause auto-inhibition of the Spt6–Rpb1 CTD and Spt6–Rpb1 linker interactions. To better understand this auto-inhibition phenomenon, we examined purified isolated tSH2 and the core of Spt6 for ability to bind the N-terminal region of Spt6 when added in *trans* using an FA assay (Figure 2). We found that tSH2 binds to the N-terminal region of Spt6 with a K_D of 0.79 ± 0.20 μM, and that the interactions of tSH2 with the N-terminal region of Spt6 and Rpb1 CTD are mutually exclusive (Supplementary Figure S2B). The tSH2 of the Spt6 domain is composed of two SH2 domains, the N-terminal (nSH2) and C-terminal (cSH2) domains, which pack tightly against each other. The nSH2 domain resembles the canonical SH2 domain, including its phosphorylation recognition binding site, while the cSH2 domain is non-canonical (19,21,23). Surprisingly, the tSH2-R1282H variant, which perturbs the binding of the nSH2 binding pocket, abolished interaction with the N-terminal region of Spt6. In contrast, the tSH2-K1355A-K1435A double variant, which perturbs the binding of cSH2 non-canonical binding pocket, has no effect on binding affinity with the N-terminal region of Spt6 ($K_D \sim 0.67 \pm 0.39$ μM; Figure 2B). This suggests that the nSH2 of Spt6 tSH2 represents an essential site that mediates the key contact to the N-terminal region of Spt6. Furthermore, we performed a binding experiment between the N-terminal region of Spt6 and the core of Spt6 (ΔN-Spt6-ΔC). Even in the absence of the tSH2 domain, we observed a binding
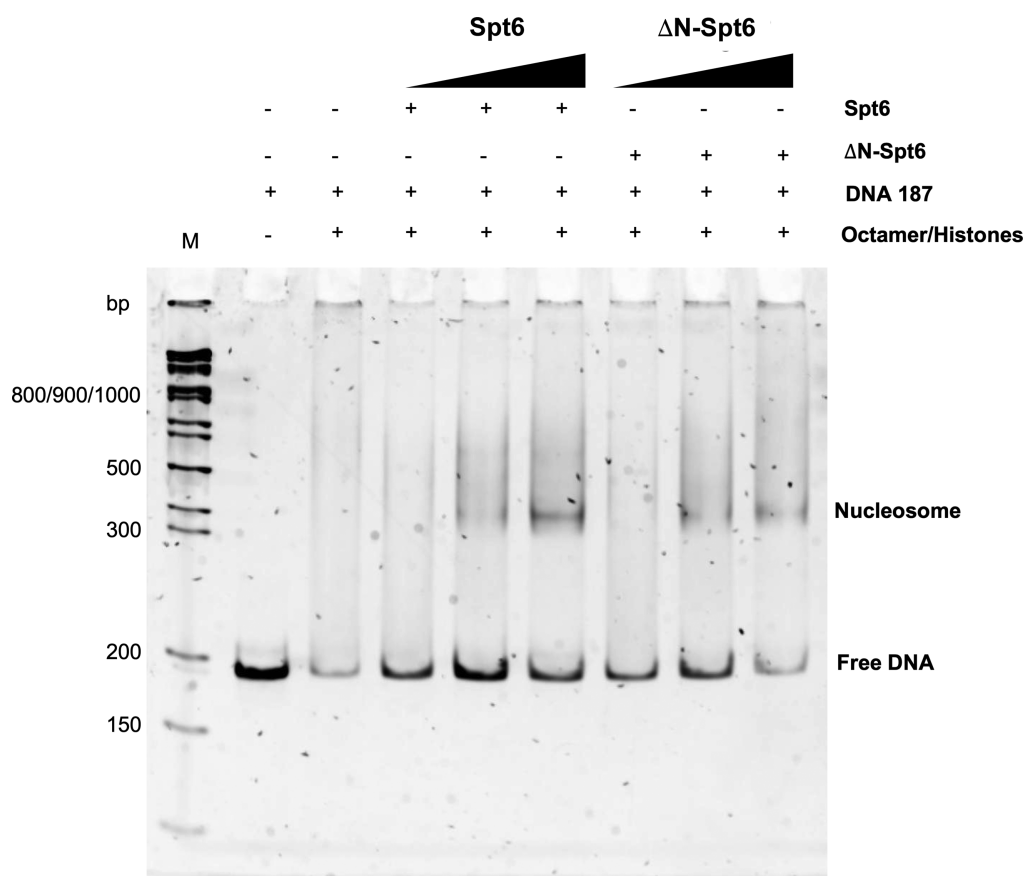
Figure 4. Spt6 promotes nucleosome assembly. EMSA reveals that Spt6 and ΔN-Spt6 are involved in nucleosome formation. All reactions included 1 pmol of DNA. Nucleosome to Spt6 molar ratios are 1:1, 1:2 and 1:4. All experiments were repeated at least twice with similar results

event with a K_D of 1.5 ± 0.7 μM (Figure 2B). This suggests that the N-terminal region of Spt6 interacts with both tSH2 and the core of Spt6. Taken together, our binding data indicate that the N-terminal region of Spt6 self-associates with the core of Spt6 and the tSH2 domain. The masking of the tSH2 domain by the N-terminal region of Spt6 autoinhibits and controls binding to the Rpb1 CTD and Rpb1 linker.

The N-terminal region of Spt6 autoregulates binding to nucleosomes

Spt6 has been shown to form stable complexes with nucleosomes only after the nucleosomes were partially destabilized by Nhp6 (26). The formation of these complexes was inhibited by Spn1, which binds to the N-terminal region of Spt6 and thus blocks an interaction between Spt6 and nucleosomes (26). To further probe the role of the N-terminal region of Spt6 in nucleosome binding, we examined purified Spt6 constructs for nucleosome and nucleosomal DNA-binding activities in an electrophoretic mobility shift assay (EMSA; Figure 3; Supplementary Figure S3). We found that Spt6 lacking the N-terminal region (ΔN-Spt6) does bind preformed nucleosomes and nucleosomal DNA in our assay, whereas Spt6 does not. The acidic IDR at the N-terminal part disrupted binding with intact nucleosome and nucleosomal DNA, even though it is involved in

histone recognition mechanisms as indicated by the MST binding assay (Supplementary Figure S4). Our data are consistent with previous observations that the full-length Spt6 does not bind double-stranded nucleic acids (18), and indicate that the N-terminal part of Spt6 autoregulates the binding events of the protein. It is possible that the autoinhibition mechanisms could be regulated by the interaction of the acidic N-terminal stretch with the fully or partially evicted basic histone proteins and other regulatory factors, and also by the interaction of tSH2 with the Pol II CTD and linker. In such a scenario, these interactions would unmask the core of Spt6 and allow for simultaneous interactions between the core of Spt6 with DNA, and the acidic N-terminal stretch with histones, which may facilitate the reassembly of nucleosomes.

The N-terminal region and core of Spt6 promote nucleosome assembly

Among other functions of Spt6 in transcription, Spt6 acts as a histone chaperone, which promotes the reassembly of nucleosomes after the passage of Pol II (14). To further investigate the mechanism of this primary function of Spt6, we examined the efficiency of Spt6 at assisting in nucleosome formation. It is known that nucleosomes do not form spontaneously under physiological salt concentrations, and a number of histone chaperones have been reported to pro-
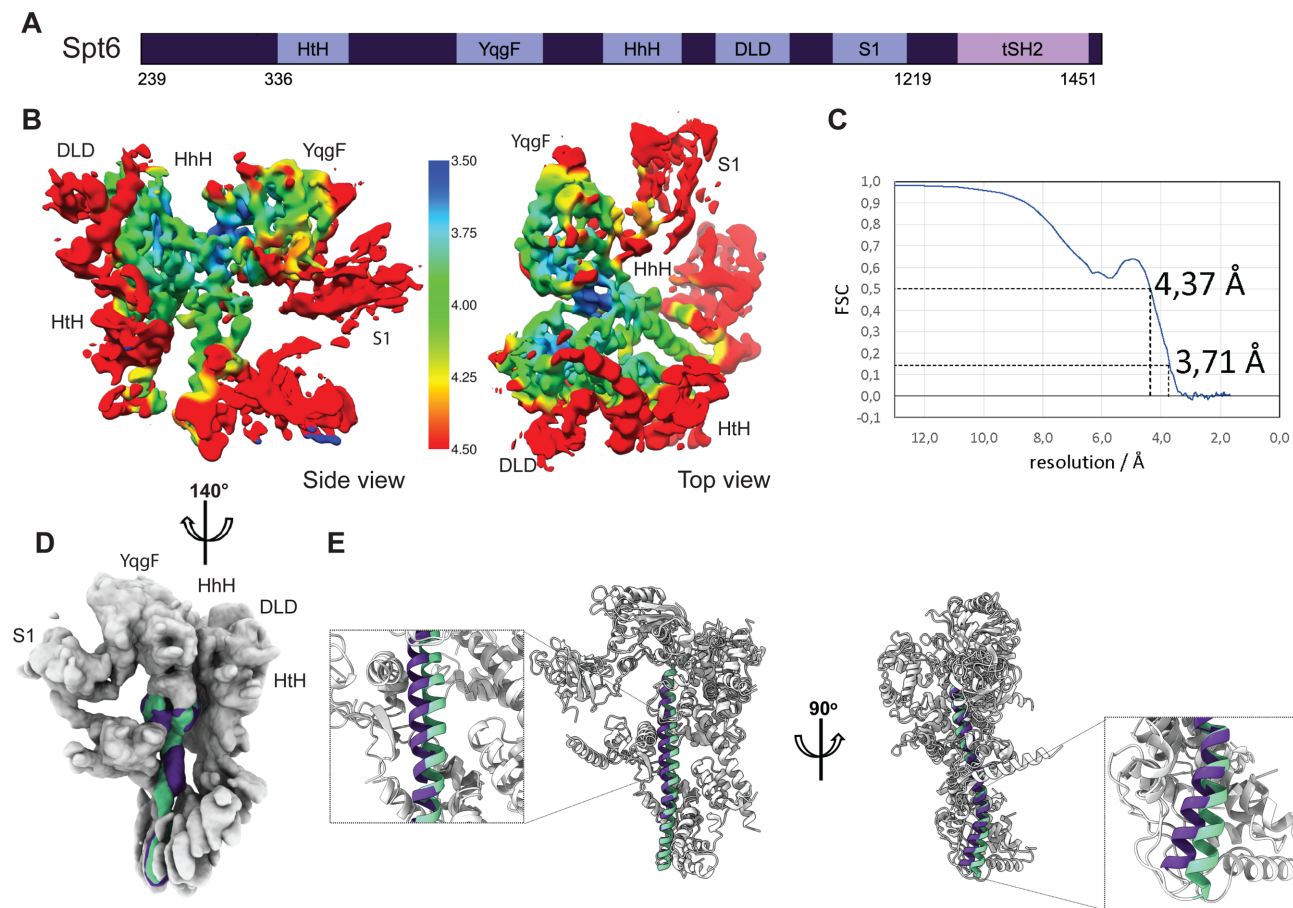
Figure 5. Cryo-EM structure of Spt6 and comparison with other structures of Spt6. (**A**) Graphical representation of construct used for Cryo-EM studies. (**B**) Local resolution estimation, shading from red to blue indicates local resolution according to colour gradient. Domains are identified. (**C**) Resolution estimated using gold-standard FSC. Resolution is given for FSC 0.143. Flexibile regions (the N-terminal part of the central helix and associated regions) were masked out. (**D**) Electron density map variability of reconstituted ΔN-Spt6. Overlay of two cryo-EM density maps highlighting extreme positions of the central helix in violet and light green. The remaining parts of Spt6 are virtually identical and are shown in grey. For detailed comparison, see Supplementary movie 1. (**E**) Overlay of unbound and Pol II-bound Spt6 structures. The cryo-EM structure of Spt6 bound to Pol II (violet, PDB ID: 6TED, (18)) and the crystal structure of the free form of Spt6 (light green, PDB ID: 3PSF, (19)). The largest conformational changes are observed for the highlighted central helix, which correspond to the variability of the cryo-EM density maps shown in (D).

mote nucleosome assembly *in vivo* (49,50). For *in vitro* experiments, nucleosomes can be reconstituted by a salt gradient dialysis method (51). This *in vitro* reconstitution method bypasses aggregation that would occur by the direct mixing of a histone octamer and DNA (52). To gain deeper insights into nucleosome formation *in vitro*, we examined purified Spt6 constructs for nucleosome assembly activity in an electrophoretic mobility shift assay (EMSA). We asked whether the capability of the N-terminal region of Spt6 to bind evicted histones and the core of Spt6 to bind DNA can promote nucleosome assembly. In the absence of Spt6, we indeed observed no spontaneous nucleosome formation by the direct mixing of purified histones with DNA (Figure 4 and Supplementary Figure S5). Interestingly, increasing the concentration of Spt6 promoted the assembly of the nucleosome (Figure 4) more effectively than Asf1 did in a control experiment (Supplementary Figure S5). The moderate level of activity of Spt6 was expected, as additional factors are required for efficient nucleosome assembly (53,54). The acidic N-terminal region of Spt6 is likely responsible for binding the highly basic histone proteins and thus shields them

from non-specific interactions, which in turn facilitates their deposition onto nucleosomal DNA, akin to other histone chaperones (55–58). However, this is not the only determinant promoting nucleosome assembly, as we observed nucleosome formation in the presence of ΔN-Spt6 (Figure 4). This suggests that the DNA-binding activities of Spt6 might also contribute to the productive formation of nucleosomes.

Cryo-EM structure of Spt6

CryoEM data were collected on a Titan Krios microscope equipped with a K2 Summit direct electron detector and subsequently processed with Relion (37) and cryoSPARC (38). After 2D and 3D classification and refinement, we obtained a 3.88 Å map of Spt6 from a set of 718 639 particles. The estimate of the average resolution improved to 3.71 Å when the regions of the structure exhibiting large flexibility (the N-terminal part of the central helix and associated regions) were masked out (Figure 5 and Supplementary Figure S6). Both maps were used to build a molecular model of Spt6. The statistics for cryo-EM data collection and pro-

Table 1. Statistics for cryo-EM data collection, processing, structural refinement and validation for Spt6

Data collection	
Microscope	FEI Titan Krios
Camera	Gatan K2 Summit direct electron camera (counting mode)
Magnification	75 000
Voltage (kV)	300
Electron dose (e^-/Å^2)	48.8
Defocus range (μm)	–1 to –2.6
Pixel size (Å)	0.828
Initial particles	2 995 892
Final particles	718 639
Model composition	
Protein residues	1153
Refinement	
Map resolution (Å)	3.71
FSC threshold	0.143
Map resolution range (Å)	
CC mask	0.72
CC volume	0.71
CC peaks	0.54
Map sharpening B-factor (Å^2)	–186.2
R.M.S. deviations	
Bond lengths (Å)	0.003
Bond angles (°)	0.768
Validation	
MolProbity score	1.62
Clashscore	6.03
Poor rotamers (%)	1
Ramachandran plot	
Favored (%)	95.84
Allowed (%)	4.16
Disallowed (%)	0

cessing, as well as for structural refinement and validation, are summarized in Table 1. The good quality and high resolution of the map allowed an accurate description at the atomic level of the Spt6 core (Figure 5). All the Spt6 core domains were resolved in the cryo-EM map and could therefore be modelled in the density, with the exception of the S1 domain, which was rigid-body docked in the density based on the S1 domain structure from the Spt6 crystal structure (19). Furthermore, no clear density was identified for the N-terminal and C-terminal tSH2 domains, suggesting a substantial flexibility of both terminal regions. Our cryo-EM map allowed us to identify previously missing regions in the crystal structure, namely a linker connecting the S1 domain and the core of Spt6. The root-mean-square-deviation (RMSD) between the cryo-EM and X-ray crystal structure is 0.99 Å.

Interestingly, the cryo-EM maps show conformational dynamics of the central helix with the largest amplitude in the N-terminal region of the helix (Figure 5). These motions are propagated to the protein chain wrapping around this helix, and are largest at the tip of an overall V shape of the Spt6 core (Supplementary Movie 1). These data suggest a rocking motion of this part, where one extreme fits well with the crystal structure of Spt6 (19) and the other extreme fits well with the cryo-EM structure of Spt6 core bound to the Rpb4/7 stalk on the Rpb1 side of Pol II (18) (Figure 5 and Supplementary Movie 1). CryoEM data also suggest that the rocking motion of the helix is coupled with motions of the S1 domain on the opposite side of the molecule (Supplementary Movie 1).

Small-angle X-ray scattering reveals conformations and dynamics of the N-terminal and tSH2 domains of Spt6

As the N-terminal and tSH2 domains were invisible to the X-ray crystallography (19) and cryo-EM analyses here and elsewhere (18,20), we collected SAXS data on the Spt6, ΔN-Spt6 and Spt6-ΔC constructs. SAXS data (summarized in Supplementary Table S2) indicate that all constructs are monomers in solution. The crystal and cryo-EM structures of the core could be docked into the calculated *ab initio* molecular envelopes without difficulty. Interestingly, D_{max} values suggest variations in particle dimensions, with the smallest value being for Spt6. To obtain a more detailed understanding about the conformation and dynamics of N-terminal and tSH2 domains, we performed SAXS-based rigid body modeling of the Spt6 constructs with CORAL (Figure 6). A total of 20 independent CORAL (44) runs were performed for each Spt6 construct to test the stability of the reconstruction. The resulting hybrid rigid body models agree well with the *ab initio* shape of the constructs and fit the experimental data well with a range of χ^2 (1.03–1.39 for Spt6; 0.98–1.03 for Spt6-ΔC; and 1.09–1.24 for ΔN-Spt6). The hybrid model of Spt6 suggests that the N-terminal domain may fold back and contact the C-terminal tSH2 domain (Figure 6B), which is in agreement with our binding data (see above) and the smallest D_{max} value among the three constructs. In the absence of the N-terminal region, the tSH2 domain samples a larger conformational space around the core of Spt6. To confirm these hybrid models, we assessed protein flexibility using SAXS data combined with the ensemble optimization method (45). EOM generates a large number of conformations using the Spt6 core and tSH2 domain structures taking the native linker and the N-terminal region into account, calculates theoretical SAXS curves for all models, and selects a mixture of conformers that fits the experimental SAXS data. The back-calculated scattering curves of the resulting ensembles fit the experimental data well with a χ^2 of 0.97, 0.97, and 1.08 for Spt6, Spt6 ΔC and ΔN-Spt6, respectively. The resulted EOM ensembles qualitatively agree with the CORAL hybrid models and show that the unstructured acidic N-terminal region of Spt6 associates with tSH2, restricting their flexibility and positioning the tSH2 domain closer to the core of Spt6. Interestingly, the communication between the N-terminal region of Spt6 and tSH2 is not spatially restricted even when Spt6 associates with Pol II (Figure 6D).

DISCUSSION

We have determined a cryo-EM structure of *S. cerevisiae* Spt6, at a resolution of ∼3.7 Å. We then combined the obtained structure with SAXS data to reveal structural information about flexible terminal regions of Spt6, which were invisible in the data from cryo-EM and X-ray crystallography (18–20). The Spt6 core structure resembles the one solved by X-ray crystallography (RMSD of 0.99 Å) and defines several regions of Spt6 that have not previously been defined in the crystal structure. CryoEM data suggest that the motions of the central helix with the largest amplitude are at the beginning of the helix. These motions are propagated to the protein chain wrapping around this helix, and
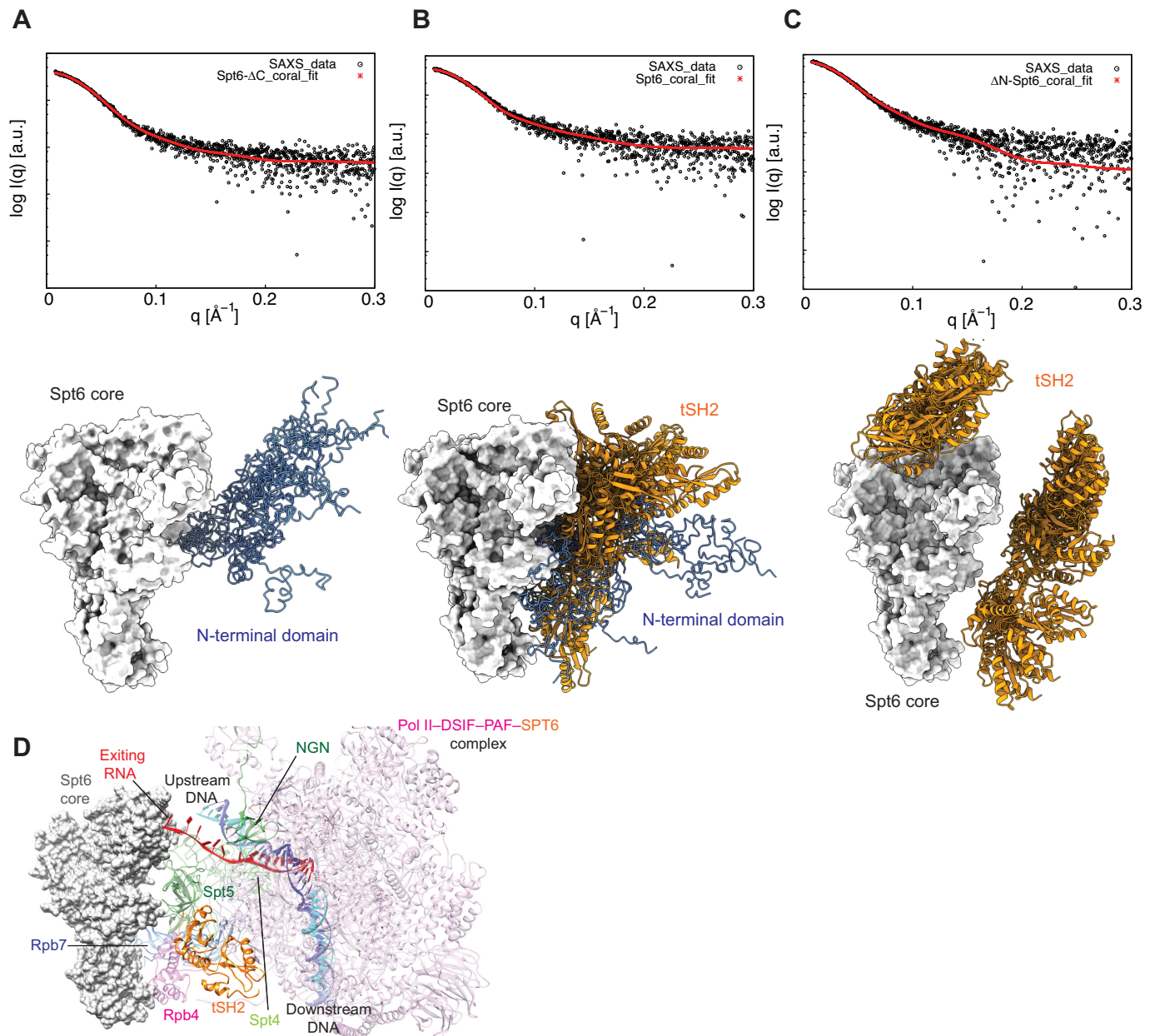
Figure 6. SAXS analysis of Spt6. Experimental SAXS profile of Spt6-ΔC (**A**, top), Spt6 (**B**, top), ΔN-Spt6 (**C**, top) and theoretical scattering (red trace) calculated for model structures shown in bottom panels. (**D**) Structure of the Pol II–DSIF–PAF–SPT6 complex (20) showing mutual orientation between the domains of SPT6 and Pol II. Pol II, pink; Rpb4, magenta; Rpb7, navy blue; Spt4, light green; Spt5, dark green; Spt6, grey; Spt6-tSH2, orange. Template and nontemplate DNA strands shown in blue and cyan, respectively; RNA, red. Color coding of Spt4, Spt5, DNA and RNA analogous as in (20) for easier orientation

are largest at the tip of an overall V shape of the Spt6 core (Supplementary Movie 1). Interestingly, the extreme positions of this motion correspond either to the structure of free Spt6 (19) or of Spt6 structure bound to Pol II (18,20). This motion is also coupled with motions of the S1 domain on the opposite side of the molecule (Supplementary Movie 1). In contrast to the flexibility of the central helix of Spt6 core and the S1 domain, the flexibility of both terminal regions is on a faster timescale and of larger amplitudes, and thus are invisible in the cryo-EM data (59,60).

The hybrid (cryo-EM–SAXS) structure supported by our binding assays indicate that the acidic N-terminal region (239–297) folds back and contacts the C-terminal tSH2 domain and the core of Spt6, leading to a model in which Spt6 is autoinhibited and requires activation. The autoinhibition mechanism explains the previous observation that Spt6 does not bind intact nucleosomes (26) or nucleosomal DNA (19). Spt6 has been shown to interact with nucleosomes only in the presence of Nhp6 (26). We hypothesize that Nhp6 promotes partial destabilization of nucleosomes

and that partially evicted basic histones could activate Spt6 binding, consistent with the fact that Spt6 can bind histones (both H2A–H2B dimers and H3–H4 tetramers) as observed here and previously (24,25). Alternatively, the Spt6 autoinhibition could be regulated by direct interaction of the acidic N-terminal region of Spt6 with basic Nhp6, similar to what has been shown for FACT (61). Furthermore, it is possible that Spt6 is activated as it undergoes dynamic conformational changes by association with Pol II. This interaction has two components–it involves the interactions between the tSH2 of Spt6 with hyper-phosphorylated Pol II CTD and/or CTD linker, and the interaction of the Spt6 core with the Rpb4/7 stalk on the Rpb1 side of Pol II (18–20,22,23). This binding-induced activation model of Spt6 is in accordance with the fact that the nucleosome reassembly is co-transcriptional, which immediately follows the passage of Pol II. The reversible phosphorylation of Pol II CTD (31,62–77) is known to recruit or repel a number of regulatory factors, including chromatin remodelers and histone chaperones, which disrupt or reassemble nucleosomes following the passage of Pol II (78).

Spt6 mutually binds DNA and histones and assists the formation of nucleosomes. The moderate level of activity of Spt6 observed in our *in vitro* assay may indicate that additional factors are required for a more efficient assembly of nucleosomes. The conformational rearrangement of Spt6 after its association with Pol II (via the Spt6 core and tSH2) and interaction with Spt4 and Spt5 (18,23,79) may be required for a more robust nucleosome assembly by Spt6 *in vitro*. *In vivo*, multiple histone chaperones, including Spt2, Spt6, Rtt106, FACT, Vps75, Asf1 and HIRA, as well as a number of chromatin remodelers and modifiers, are implicated in the reestablishment of chromatin structure and maintenance of epigenetic information, after the passage of RNA polymerase II (14,80–86). However, is it unclear whether these histone chaperones act together or in distinct settings. Recent cryo-EM structures of human FACT in complex with partially assembled subnucleosomes showed that FACT is engaged in extensive interactions with nucleosomal DNA and all histone variants, which suggests that FACT maintains chromatin integrity during polymerase passage by stabilizing intermediate subnucleosomal states and promoting nucleosome reassembly (56). As Spt6 also binds nucleosomal DNA and histones, it is possible that it utilizes a similar mechanism to promote nucleosome reassembly. Furthermore, the Spt6-mediated nucleosome reassembly can be regulated by Spn1 that is able to sequester the N-terminal region of Spt6 (26,87) in a phosphorylation-dependent manner (88). It is also possible, that in addition to the stretch of amino acids (239–297) that autoinhibits Spt6 binding activity, the first 238 amino acids, which are highly acidic and subject to phosphorylation by casein kinase II (88), may also contribute to Spt6 function. In summary, we determined the structural basis for the cooperation between the intrinsically disordered and ordered regions of Spt6, which regulates nucleosome and Pol II CTD binding, as well as nucleosome assembly. To elucidate the precise structural mechanism of Spt6-mediated nucleosome reassembly, further structural studies of Spt6 bound to histones/nucleosome and Pol II-Spt4/5 are needed.

DATA AVAILABILITY

SUPPLEMENTARY DATA

Supplementary Data are available at NAR Online.

ACKNOWLEDGEMENTS

FUNDING

REFERENCES

1. Clark-Adams,C.D. and Winston,F. (1987) The SPT6 gene is essential for growth and is required for delta-mediated transcription in saccharomyces cerevisiae. *Mol. Cell. Biol.*, **7**, 679–686.
2. Endoh,M., Zhu,W., Hasegawa,J., Watanabe,H., Kim,D.-K., Aida,M., Inukai,N., Narita,T., Yamada,T., Furuya,A. *et al.* (2004) Human spt6 stimulates transcription elongation by RNA polymerase II in vitro. *Mol. Cell. Biol.*, **24**, 3324–3336.
3. Ardehali,M.B., Yao,J., Adelman,K., Fuda,N.J., Petesch,S.J., Webb,W.W. and Lis,J.T. (2009) Spt6 enhances the elongation rate of RNA polymerase II in vivo. *EMBO J.*, **28**, 1067–1077.
4. Baniahmad,C., Nawaz,Z., Baniahmad,A., Gleeson,M.A.G., Tsai,M.J. and O'Malley,B.W. (1995) Enhancement of human estrogen receptor activity by SPT6: a potential coactivator. *Mol. Endocrinol.*, **9**, 34–43.
5. Yoh,S.M., Cho,H., Pickle,L., Evans,R.M. and Jones,K.A. (2007) The spt6 SH2 domain binds Ser2-P RNAPII to direct Iws1-dependent mRNA splicing and export. *Genes Dev.*, **21**, 160–174.
6. Adkins,M.W. and Tyler,J.K. (2006) Transcriptional activators are dispensable for transcription in the absence of Spt6-mediated chromatin reassembly of promoter regions. *Mol. Cell*, **21**, 405–416.

7. Obara,E.A.A., Aguilar-Morante,D., Rasmussen,R.D., Frias,A., Vitting-Serup,K., Lim,Y.C., Elbæk,K.J., Pedersen,H., Vardouli,L., Jensen,K.E. *et al.* (2020) SPT6-driven error-free DNA repair safeguards genomic stability of glioblastoma cancer stem-like cells. *Nat. Commun.*, **11**, 4709.

8. Dronamraju,R., Hepperla,A.J., Shibata,Y., Adams,A.T., Magnuson,T., Davis,I.J. and Strahl,B.D. (2018) Spt6 association with RNA polymerase II directs mRNA turnover during transcription. *Mol. Cell*, **70**, 1054–1066.

9. Bobkov,G.O.M., Huang,A., van den Berg,S.J.W., Mitra,S., Anselm,E., Lazou,V., Schunter,S., Feederle,R., Imhof,A., Lusser,A. *et al.* (2020) Spt6 is a maintenance factor for centromeric CENP-A. *Nat. Commun.*, **11**, 2919.

10. Gopalakrishnan,R., Marr,S.K., Kingston,R.E. and Winston,F. (2019) A conserved genetic interaction between spt6 and set2 regulates H3K36 methylation. *Nucleic Acids Res.*, **47**, 3888–3903.

11. Youdell,M.L., Kizer,K.O., Kisseleva-Romanova,E., Fuchs,S.M., Duro,E., Strahl,B.D. and Mellor,J. (2008) Roles for ctk1 and spt6 in regulating the different methylation states of histone H3 lysine 36. *Mol. Cell. Biol.*, **28**, 4915–4926.

12. DeGennaro,C.M., Alver,B.H., Marguerat,S., Stepanova,E., Davis,C.P., Bahler,J., Park,P.J. and Winston,F. (2013) Spt6 regulates intragenic and antisense transcription, nucleosome positioning, and histone modifications genome-wide in fission yeast. *Mol. Cell. Biol.*, **33**, 4779–4792.

13. Doris,S.M., Chuang,J., Viktorovskaya,O., Murawska,M., Spatt,D., Churchman,L.S. and Winston,F. (2018) Spt6 is required for the fidelity of promoter selection. *Mol. Cell*, **72**, 687–699.

14. Jeronimo,C., Poitras,C. and Robert,F. (2019) Histone recycling by FACT and spt6 during transcription prevents the scrambling of histone modifications. *Cell Rep.*, **28**, 1206–1218.

15. Hainer,S.J., Pruneski,J.A., Mitchell,R.D., Monteverde,R.M. and Martens,J.A. (2011) Intergenic transcription causes repression by directing nucleosome assembly. *Genes Dev.*, **25**, 29–40.

16. Kaplan,C.D., Laprade,L. and Winston,F. (2003) Transcription elongation factors repress transcription initiation from cryptic sites. *Science*, **301**, 1096–1099.

17. Mayer,A., Lidschreiber,M., Siebert,M., Leike,K., Söding,J. and Cramer,P. (2010) Uniform transitions of the general RNA polymerase II transcription complex. *Nat. Struct. Mol. Biol.*, **17**, 1272–1278.

18. Vos,S.M., Farnung,L., Boehning,M., Wigge,C., Linden,A., Urlaub,H. and Cramer,P. (2018) Structure of activated transcription complex pol II–DSIF–PAF–SPT6. *Nature*, **560**, 607–612.

19. Close,D., Johnson,S.J., Sdano,M.A., McDonald,S.M., Robinson,H., Formosa,T. and Hill,C.P. (2011) Crystal structures of the s. cerevisiae spt6 core and C-terminal tandem SH2 domain. *J. Mol. Biol.*, **408**, 697–713.

20. Vos,S.M., Farnung,L., Linden,A., Urlaub,H. and Cramer,P. (2020) Structure of complete pol II–DSIF–PAF–SPT6 transcription complex reveals RTF1 allosteric activation. *Nat. Struct. Mol. Biol.*, **27**, 668–677.

21. Sun,M., Larivière,L., Dengl,S., Mayer,A. and Cramer,P. (2010) A tandem SH2 domain in transcription elongation factor spt6 binds the phosphorylated RNA polymerase II C-terminal repeat domain (CTD). *J. Biol. Chem.*, **285**, 41597–41603.

22. Sdano,M.A., Fulcher,J.M., Palani,S., Chandrasekharan,M.B., Parnell,T.J., Whitby,F.G., Formosa,T. and Hill,C.P. (2017) A novel SH2 recognition mechanism recruits spt6 to the doubly phosphorylated RNA polymerase II linker at sites of transcription. *Elife*, **6**, e28723.

23. Brázda,P., Krejčíková,M., Kasiliauskaite,A., Šmiřáková,E., Klumpler,T., Vácha,R., Kubíček,K. and Štefl,R. (2020) Yeast spt6 reads multiple phosphorylation patterns of RNA polymerase II C-Terminal domain in vitro. *J. Mol. Biol.*, **432**, 4092–4107.

24. Bortvin,A. and Winston,F. (1996) Spt6p controls chromatin. *Science*, **272**, 473–477.

25. McCullough,L., Connell,Z., Petersen,C. and Formosa,T. (2015) The abundant histone chaperones spt6 and FACT collaborate to assemble, inspect, and maintain chromatin structure in saccharomyces cerevisiae. *Genetics*, **201**, 1030–1045.

26. McDonald,S.M., Close,D., Xin,H., Formosa,T. and Hill,C.P. (2010) Structure and biological importance of the spn1-spt6 interaction, and its regulatory role in nucleosome binding. *Mol. Cell*, **40**, 725–735.

27. Klock,H.E., Koesema,E.J., Knuth,M.W. and Lesley,S.A. (2008) Combining the polymerase incomplete primer extension method for cloning and mutagenesis with microscreening to accelerate structural genomics efforts. *Proteins Struct. Funct. Genet.*, **71**, 982–994.

28. Ivić,N., Groschup,B., Bilokapić,S. and Halić,M. (2016) Simplified method for rapid purification of soluble histones. *Croat. Chem. Acta*, **89**, 153–162.

29. Bilokapic,S. and Halic,M. (2019) Nucleosome and ubiquitin position set2 to methylate H3K36. *Nat. Commun.*, **10**, 3795.

30. Bilokapic,S., Strauss,M. and Halic,M. (2018) Structural rearrangements of the histone octamer translocate DNA. *Nat. Commun.*, **9**, 1330.

31. Kubicek,K., Cerna,H., Holub,P., Pasulka,J., Hrossova,D., Loehr,F., Hofr,C., Vanacova,S. and Stefl,R. (2012) Serine phosphorylation and proline isomerization in RNAP II CTD control recruitment of nrdl. *Genes Dev.*, **26**, 1891–1896.

32. Mastronarde,D.N. (2005) Automated electron microscope tomography using robust prediction of specimen movements. *J. Struct. Biol.*, **152**, 36–51.

33. Zheng,S.Q., Palovcak,E., Armache,J.P., Verba,K.A., Cheng,Y. and Agard,D.A. (2017) MotionCor2: anisotropic correction of beam-induced motion for improved cryo-electron microscopy. *Nat. Methods*, **14**, 331–332.

34. Zhang,K. (2016) Gctf: Real-time CTF determination and correction. *J. Struct. Biol.*, **193**, 1–12.

35. Tang,G., Peng,L., Baldwin,P.R., Mann,D.S., Jiang,W., Rees,I. and Ludtke,S.J. (2007) EMAN2: an extensible image processing suite for electron microscopy. *J. Struct. Biol.*, **157**, 38–46.

36. Wagner,T., Merino,F., Stabrin,M., Moriya,T., Antoni,C., Apelbaum,A., Hagel,P., Sitsel,O., Raisch,T., Prumbaum,D. *et al.* (2019) SPHIRE-crYOLO is a fast and accurate fully automated particle picker for cryo-EM. *Commun. Biol.*, **2**, 218.

37. Zivanov,J., Nakane,T., Forsberg,B.O., Kimanius,D., Hagen,W.J., Lindahl,E. and Scheres,S.H. (2018) New tools for automated high-resolution cryo-EM structure determination in RELION-3. *Elife*, **7**, e42166.

38. Punjani,A., Rubinstein,J.L., Fleet,D.J. and Brubaker,M.A. (2017) CryoSPARC: algorithms for rapid unsupervised cryo-EM structure determination. *Nat. Methods*, **14**, 290–296.

39. Emsley,P., Lohkamp,B., Scott,W.G. and Cowtan,K. (2010) Features and development of coot. *Acta Crystallogr. Sect. D Biol. Crystallogr.*, **66**, 486–501.

40. Liebschner,D., Afonine,P.V., Baker,M.L., Bunkoczi,G., Chen,V.B., Croll,T.I., Hintze,B., Hung,L.W., Jain,S., McCoy,A.J. *et al.* (2019) Macromolecular structure determination using X-rays, neutrons and electrons: recent developments in phenix. *Acta Crystallogr. Sect. D Struct. Biol.*, **75**, 861–877.

41. Croll,T.I. (2018) ISOLDE: a physically realistic environment for model building into low-resolution electron-density maps. *Acta Crystallogr. Sect. D Struct. Biol.*, **74**, 519–530.

42. Williams,C.J., Headd,J.J., Moriarty,N.W., Prisant,M.G., Videau,L.L., Deis,L.N., Verma,V., Keedy,D.A., Hintze,B.J., Chen,V.B. *et al.* (2018) MolProbity: more and better reference data for improved all-atom structure validation. *Protein Sci.*, **27**, 293–315.

43. Franke,D., Petoukhov,M.V., Konarev,P.V., Panjkovich,A., Tuukkanen,A., Mertens,H.D.T., Kikhney,A.G., Hajizadeh,N.R., Franklin,J.M., Jeffries,C.M. *et al.* (2017) ATSAS 2.8: a comprehensive data analysis suite for small-angle scattering from macromolecular solutions. *J. Appl. Crystallogr.*, **50**, 1212–1225.

44. Petoukhov,M.V., Franke,D., Shkumatov,A.V., Tria,G., Kikhney,A.G., Gajda,M., Gorba,C., Mertens,H.D.T., Konarev,P.V. and Svergun,D.I. (2012) New developments in the ATSAS program package for small-angle scattering data analysis. *J. Appl. Crystallogr.*, **45**, 342–350.

45. Tria,G., Mertens,H.D.T., Kachala,M. and Svergun,D.I. (2015) Advanced ensemble modelling of flexible macromolecules using X-ray solution scattering. *IUCrJ*, **2**, 207–217.

46. Pettersen,E.F., Goddard,T.D., Huang,C.C., Meng,E.C., Couch,G.S., Croll,T.I., Morris,J.H. and Ferrin,T.E. (2021) UCSF chimerax: structure visualization for researchers, educators, and developers. *Protein Sci.*, **30**, 70–82.

47. Burugula,B.B., Jeronimo,C., Pathak,R., Jones,J.W., Robert,F. and Govind,C.K. (2014) Histone deacetylases and phosphorylated

polymerase II C-Terminal domain recruit spt6 for cotranscriptional histone reassembly. *Mol. Cell. Biol.*, **34**, 4115–4129.

48. Mayer,A., Heidemann,M., Lidschreiber,M., Schreieck,A., Sun,M., Hintermair,C., Kremmer,E., Eick,D. and Cramer,P. (2012) CTD tyrosine phosphorylation impairs termination factor recruitment to RNA polymerase II. *Science.*, **336**, 1723–1725.

49. Pardal,A.J., Fernandes-Duarte,F. and Bowman,A.J. (2019) The histone chaperoning pathway: from ribosome to nucleosome. *Essays Biochem.*, **63**, 29–43.

50. Hammond,C.M., Strømme,C.B., Huang,H., Patel,D.J. and Groth,A. (2017) Histone chaperone networks shaping chromatin function. *Nat. Rev. Mol. Cell Biol.*, **18**, 141–158.

51. Dyer,P.N., Edayathumangalam,R.S., White,C.L., Bao,Y., Chakravarthy,S., Muthurajan,U.M. and Luger,K. (2003) Reconstitution of nucleosome core particles from recombinant histones and DNA. *Methods Enzymol.*, **375**, 23–44.

52. Muthurajan,U., Mattiroli,F., Bergeron,S., Zhou,K., Gu,Y., Chakravarthy,S., Dyer,P., Irving,T. and Luger,K. (2016) In vitro chromatin assembly: strategies and quality control. In: *Methods in Enzymology*. Academic Press Inc., Vol. 573, pp. 3–41.

53. Orphanides,G., LeRoy,G., Chang,C.H., Luse,D.S. and Reinberg,D. (1998) FACT, a factor that facilitates transcript elongation through nucleosomes. *Cell*, **92**, 105–116.

54. Ivanovska,I., Jacques,P.-E., Rando,O.J., Robert,F. and Winston,F. (2011) Control of chromatin structure by spt6: different consequences in coding and regulatory regions. *Mol. Cell. Biol.*, **31**, 531–541.

55. Warren,C. and Shechter,D. (2017) Fly fishing for histones: catch and release by histone chaperone intrinsically disordered regions and acidic stretches. *J. Mol. Biol.*, **429**, 2401–2426.

56. Liu,Y., Zhou,K., Zhang,N., Wei,H., Tan,Y.Z., Zhang,Z., Carragher,B., Potter,C.S., D'Arcy,S. and Luger,K. (2019) FACT caught in the act of manipulating the nucleosome. *Nature*, **577**, 426–431.

57. Zhou,K., Liu,Y. and Luger,K. (2020) Histone chaperone FACT FAcilitates chromatin transcription: mechanistic and structural insights. *Curr. Opin. Struct. Biol.*, **65**, 26–32.

58. Wang,T., Liu,Y., Edwards,G., Krzizike,D., Scherman,H. and Luger,K. (2018) The histone chaperone FACT modulates nucleosome structure by tethering its components. *Life Sci. Alliance*, **1**, e201800107.

59. Lyumkis,D. (2019) Challenges and opportunities in cryo-EM single-particle analysis. *J. Biol. Chem.*, **294**, 5181–5197.

60. Punjani,A. and Fleet,D.J. (2021) 3D variability analysis: directly resolving continuous flexibility and discrete heterogeneity from single particle cryo-EM images. J. Struct. Biol., **213**, 107702.

61. Sivkina,A.L., Karlova,M.G., Valieva,M.E., McCullough,L.L., Formosa,T., Shaytan,A.K., Feofanov,A.V., Kirpichnikov,M.P., Sokolova,O.S. and Studitsky,V.M. (2022) Electron microscopy analysis of ATP-independent nucleosome unfolding by FACT. *Commun. Biol.***5**, 2.

62. Buratowski,S. (2003) The CTD code. *Nat. Struct. Biol.*, **10**, 679–680.

63. Jasnovidova,O., Klumpler,T., Kubicek,K., Kalynych,S., Plevka,P. and Stefl,R. (2017) Structure and dynamics of the RNAPII CTDsome with rtt103. *Proc. Natl. Acad. Sci. U.S.A.*, **114**, 11133–11138.

64. Jasnovidova,O., Krejcikova,M., Kubicek,K. and Stefl,R. (2017) Structural insight into recognition of phosphorylated threonine-4 of RNA polymerase II C-terminal domain by rtt103p . *EMBO Rep.*, **18**, 906–913.

65. Harlen,K.M. and Churchman,L.S. (2017) The code and beyond: transcription regulation by the RNA polymerase II carboxy-terminal domain. *Nat. Rev. Mol. Cell Biol.*, **18**, 263–273.

66. Yurko,N.M. and Manley,J.L. (2018) The RNA polymerase II CTD "orphan" residues: emerging insights into the functions of tyr-1, thr-4, and Ser-7. *Transcription*, **9**, 30–40.

67. Lyons,D.E., McMahon,S. and Ott,M. (2020) A combinatorial view of old and new RNA polymerase II modifications. *Transcription*, **11**, 66–82.

68. Bae,H.J., Dubarry,M., Jeon,J., Soares,L.M., Dargemont,C., Kim,J., Geli,V. and Buratowski,S. (2020) The set1 N-terminal domain and swd2 interact with RNA polymerase II CTD to recruit COMPASS. *Nat. Commun.*, **11**, 2181.

69. Han,Z., Jasnovidova,O., Haidara,N., Tudek,A., Kubicek,K., Libri,D., Stefl,R. and Porrua,O. (2020) Termination of non-coding transcription in yeast relies on both an RNA pol II CTD interaction domain and a CTD-mimicking region in sen1. *EMBO J.*, **39**, e101548.

70. Jasnovidova,O. and Stefl,R. (2013) The CTD code of RNA polymerase II: a structural view. *Wiley Interdiscip. Rev. RNA*, **4**, 1–16.

71. Eick,D. and Geyer,M. (2013) The RNA polymerase II carboxy-terminal domain (CTD) code. *Chem. Rev.*, **113**, 8456–8490.

72. Heidemann,M. and Eick,D. (2012) Tyrosine-1 and threonine-4 phosphorylation marks complete the RNA polymerase II CTD phospho-code. *RNA Biol.*, **9**, 1144–1146.

73. Kubíček,K., Pasulka,J., Černá,H., Löhr,F. and Štefl,R. (2011) 1H, 13C, and 15N resonance assignments for the CTD-interacting domain of nrd1 bound to Ser5-phosphorylated CTD of RNA polymerase II. *Biomol. NMR Assign.*, **5**, 203–205.

74. Napolitano,G., Lania,L. and Majello,B. (2014) RNA polymerase II CTD modifications: how many tales from a single tail. *J. Cell. Physiol.*, **229**, 538–544.

75. Jeronimo,C., Collin,P. and Robert,F. (2016) The RNA polymerase II CTD: the increasing complexity of a low-complexity protein domain. *J. Mol. Biol.*, **428**, 2607–2622.

76. Zaborowska,J., Egloff,S. and Murphy,S. (2016) The pol II CTD: new twists in the tail. *Nat. Struct. Mol. Biol.*, **23**, 771–777.

77. Nemec,C.M., Yang,F., Gilmore,J.M., Hintermair,C., Ho,Y.H., Tseng,S.C., Heidemann,M., Zhang,Y., Florens,L., Gasch,A.P. *et al.* (2017) Different phosphoisoforms of RNA polymerase II engage the rtt103 termination factor in a structurally analogous manner. *Proc. Natl. Acad. Sci. U.S.A.*, **114**, E3944–E3953.

78. Venkatesh,S. and Workman,J.L. (2015) Histone exchange, chromatin structure and the regulation of transcription. *Nat. Rev. Mol. Cell Biol.*, **16**, 178–189.

79. Ehara,H., Yokoyama,T., Shigematsu,H., Yokoyama,S., Shirouzu,M. and Sekine,S.I. (2017) Structure of the complete elongation complex of RNA polymerase II with basal factors. *Science*, **357**, 921–924.

80. Chen,S., Rufiange,A., Huang,H., Rajashankar,K.R., Nourani,A. and Patel,D.J. (2015) Structure–function studies of histone H3/H4 tetramer maintenance during transcription by chaperone Spt2. *Genes Dev.*, **29**, 1326–1340.

81. Mei,Q., Xu,C., Gogol,M., Tang,J., Chen,W., Yu,X., Workman,J.L. and Li,S. (2019) Set1-catalyzed H3K4 trimethylation antagonizes the HIR/Asf1/Rtt106 repressor complex to promote histone gene expression and chronological life span. *Nucleic Acids Res.*, **47**, 3434–3449.

82. Akhavantabib,N., Krzizike,D.D., Neumann,V. and D'Arcy,S. (2020) Stoichiometry of rtt109 complexes with vps75 and histones H3–H4. *Life Sci. Alliance*, **3**, e202000771.

83. Srivastava,D.K., Gunjan,S., Das,C., Seshadri,V. and Roy,S. (2021) Structural insights into histone chaperone asf1 and its characterization from plasmodium falciparum. *Biochem. J.*, **478**, 1117–1136.

84. Wang,P., Yang,W., Zhao,S. and Nashun,B. (2021) Regulation of chromatin structure and function: insights into the histone chaperone FACT. *Cell Cycle*, **20**, 465–479.

85. Formosa,T. and Winston,F. (2021) The role of FACT in managing chromatin: disruption, assembly, or repair?*Nucleic Acids Res.*, **48**, 11929–11941.

86. Viktorovskaya,O., Chuang,J., Jain,D., Reim,N.I., López-Rivera,F., Murawska,M., Spatt,D., Stirling Churchman,L., Park,P.J. and Winston,F. (2021) Essential histone chaperones collaborate to regulate transcription and chromatin integrity. *Genes Dev.*, **35**, 698–712.

87. Reim,N.I., Chuang,J., Jain,D., Alver,B.H., Park,P.J. and Winston,F. (2020) The conserved elongation factor spn1 is required for normal transcription, histone modifications, and splicing in saccharomyces cerevisiae. *Nucleic Acids Res.*, **48**, 10241–10258.

88. Dronamraju,R., Kerschner,J.L., Peck,S.A., Hepperla,A.J., Adams,A.T., Hughes,K.D., Aslam,S., Yoblinski,A.R., Davis,I.J., Mosley,A.L. *et al.* (2018) Casein kinase II phosphorylation of spt6 enforces transcriptional fidelity by maintaining spn1-spt6 interaction. *Cell Rep*, **25**, 3476–3489.